3D printing of powdered activated carbon monoliths: Effect of structuring on physicochemical and mechanical properties and its influence on the adsorption performance

Jair Fernando Rangel-Sequeda a, Margarita Loredo-Cancino a, Vicente Ismael Agueda Mate b, David Alejandro De Haro-Del Rio a, Nancy Elizabeth Davila-Guzman a

a Facultad de Ciencias Químicas, Universidad Autonoma de Nuevo Leon, San Nicolas de los Garza, Mexico

b Department of Chemical Engineering, Universidad Complutense de Madrid, Madrid, Spain

ABSTRACT

Herein, a methodology for 3D printing of activated carbon powders in monolithic form using direct ink writing and carboxymethylcellulose as binder is reported, along with the effect on their physicochemical and mechanical properties. Monoliths with different wall diameters (0.42, 0.62, and 0.82 mm) and infill percentages (30%, 50%, and 70%) were designed and manufactured. The monoliths were heat-treated under a nitrogen atmosphere at 400 ◦C and 600 ◦C to remove the volatile material from the binder used. The monoliths showed a decrease in dimension of less than 8% from their designed values, attributed to the volatilization of water present in the binder solution in the drying and heat-treatment process. The printed monoliths presented pore distributions similar to those of their powdered counterparts. The isoelectric point of the monoliths increased relative to that of the powdered material and became more basic as the heat treatment temperature increased. The monoliths presented compressive strengths from 0.58 to 3.53 MPa. The analysis of variance of the compressive strength showed that the wall diameter and temperature are the most influential treatment parameters. The printed monoliths exhibited similar CO2 adsorption capacity (0.37 mol Kg− 1 at 10 kPa and 25 ◦C) compared to the powder precursor. Fixed bed tests demonstrated that the 3D printed monoliths enhanced the mass transfer compared to conventionally extruded pellets with same wall diameter.

1. Introduction

The structuring of materials has gained increasing interest in recent years due to improvements in the kinetic and engineering factors associated with separation or catalysis processes [1-3]. Compared to traditional structures such as pellets or beads, monolithic structures have presented better performance in terms of pressure drop, adsorption enthalpy effects, external heat integration (for temperature swing adsorption (TSA)), mechanical stability, optimization of gas flow paths to reaction sites, mass, and energy transfer, among others [4,5]. Different extrusion methods for materials have been reported in the literature and can be classified into two types [6]. The first type involves the impregnation of materials into inert structures by either washing or hydrothermal treatment [7-9]. However, the resulting configurations have a low content of adsorbent material and exhibit coating adhesion problems. The second type, active structuring, solves this problem but necessitates the inclusion of a binder system [10,11], which can change the textural and surface chemical properties of the adsorbent material. The main active structuring methods are mechanical extrusion [12], reverse replication [13], and dry gel conversion [14]; however, these methods can produce only limited structures [15]. Additive manufacturing, better known as 3D printing, overcomes these disadvantages and can create complex geometries that are impossible to reproduce by conventional active methods; this approach is commonly used to investigate and evaluate new structures [16,17]. Recent research on 3D printed carbon materials and zeolites has shown promising results for CO2 capture, gas separation, catalysis, microbial fuel cell, and energy storage [18-22]. 3D printing techniques such as stereolithography (SLA) have produced monolithic carbon periodic structures [23-26]. Although these structures present complex and defined geometries, they are based on photosensitive resins whose final properties of the monolith depend on the thermal treatments after printing. On the other hand, techniques such as direct ink deposition [27,28] allow the structuring of powdered materials already synthesized and optimized for specific uses. However, solid materials in powder form need to be mixed with viscous solutions to create a paste that can be deposited smoothly in 3D printers and results in a robust structure that preserves the properties of the precursor. For inorganic porous solids, clays or silica based binders are often used [10] and require high-temperature treatment to obtain a solid and robust structure. Alternatively, polymeric binders allow rigid structures to be obtained without needing high-temperature treatment [16] and provide an exciting option when the selected porous material cannot withstand the aggressive heat treatment. Regufe et al. [21] reported the manufacture of honeycomb monoliths using a 13X zeolite compound, activated carbon, and carboxymethylcellulose as binder. Nevertheless, reports on how structuring by 3D printing of activated carbons powder by carboxymethylcellulose influences their

physical and chemical properties, possible mechanical resistance, and the performance of CO2 adsorption are lacking. This study proposes monolithic structuring by directly printing 3D ink using a low-cost extrusion system and renewable origin precursors. Activated carbon of coconut husks (MEGAPOL LS325) was used as an adsorbent powder material and carboxymethyl cellulose as a binder. The effect on the adsorbent material's physical-chemical properties and mechanical resistance was studied by varying the structure and calcination temperature. Likewise, the efficiency of monolithic structures in separating CO2 is compared to the structure pellets form.

2. Materials and methods

2.1. 3D printing of monoliths

A commercial activated carbon (AC), MEGAPOL LS325 (Carbotecnia, Mexico), was used as a solid material. The AC was ground and sieved to pass through a 400 mesh (dp less than 0.034 mm). The printing ink formulation was based on an aqueous sodium carboxymethyl cellulose (CMC) solution (high viscosity, Sigma Aldrich) with a concentration of 3% w/w. For the preparation of the ink, AC and CMC were added with a mass ratio of 1:2 and mixed manually until a homogeneous paste was achieved. Then, the ink was loaded into a 20 mL syringe and manually extruded. The extrusion process was repeated four times to obtain a paste with homogeneous rheological properties. 3D printing of the ink (AC-CMC) was performed by direct writing using nozzles of different diameters (0.42, 0.62, and 0.82 mm) coupled to an XYZ print head. A mechanical piston microextruder (Fig. 1) based on several approaches [29,30] was used to control overflow from the ink through the nozzle. The ink was printed in cylindrical structures stacked layer by layer with a contact angle between layers of 90◦, a layer height of 50% of the nozzle diameter, and different infill percentages (30%, 50%, and 70%). Cylindrical structures with diameters from 5 to 20 mm and heights from 3 to 30 mm were printed. The monoliths were dried at ambient temperature and heat-treated under a nitrogen atmosphere at 400 ◦C and 600 ◦C to remove the volatile material from the binder used. The finished monoliths were named ACm_A_B_C, where A is the nozzle diameter, B is the infill percentage, and C is the heat treatment temperature.

2.2. Characterization

The morphological properties were determined by optical and electronic microscopy using a scanning electron microscope (SEM) (JSM6701 F, JOEL) at different magnifications. The porosity of the materials was characterized by the nitrogen adsorption/desorption equilibrium isotherm method at − 196.15 ◦C using a static volumetric analyzer (ASAP 2020 Plus, Micromeritics). All samples were

degassed for 12 h at 120 ◦C. The specific surface area (SBET) was estimated with the Brunauer–Emmett–Teller (BET) method in a relative pressure range between 0.05 and 0.25. The pore size distribution, micropore volume (Vic), and average diameter (Dav) were determined by the nonlocal density functional theory (NLDFT) model. The total volume of nitrogen adsorbed (Vt) was determined at a relative pressure of 0.95. The isoelectric point and surface charge distribution were determined by a titration method reported by [31]. In addition, X-ray photoelectron spectroscopy (XPS) analysis was performed on a Thermo Scientific ESCALAB250xi to characterize the chemical bonding states of the elements present. The monolithic mechanical strength was determined according to ASTM C695–15 [32]. A hydraulic press coupled to a 25 kN measuring cell was used to detect the force needed to collapse the structures (5980 Series Universal Testing Systems, Instron).

2.3. Experimental design

A multilevel factorial design (Table 1) was used to determine the influence of geometry and heat treatment on the mechanical strength of the monolithic materials. Analysis of variance was used to measure the magnitude of the effects of the factors on the response variables. The adjusted determination coefficient (R2 Adj) was used to measure the proportion of the total observed variability described by the model [33]. The factorial model was used to build the response variable surfaces and find the maximal value of responses by using Design-Expert software (version 11.1.2, Stat-Ease, Inc., USA).

2.4. Carbon dioxide and nitrogen adsorption

2.4.1. Volumetric adsorption

The single-component adsorption isotherms of CO2 and N2 on the AC were measured volumetrically in the Micromeritics ASAP-2010. Three temperatures were evaluated, 25, 40, and 65 ◦C, up to a pressure of 1.2 × 105 Pa for each gas. The material was initially outgassed at 120 ◦C under vacuum for one night. The adsorption temperatures were achieved by using a Dewar flask with a circulating jacket connected to a thermostatic bath. The free space of the system was determined by using helium. The degasification procedure was repeated on the same sample between measurements for 2 h. The quantity of gas adsorbed was determined using the universal gas law. A non-linear fitting to the experimental data was used to determine the parameters of the temperature-dependent Langmuir isotherm (Eq. 1) using the multiple fit option of the Origin® software, where qi is the adsorption capacity in mol kg− 1 , qmax ,i is the maximum capacity in mol kg− 1 , KL,i is the adsorption constant of Langmuir in Pa− 1 , which is function of temperature according to Arrhenius equation. Pi is the partial pressure in the gas

phase in Pa, T is temperature of system in K and ΔHads,i is the heat of adoption in J mol− 1 . The affinity of the material for the different adsorbents through the Henry adsorption constants (KH,i) have been calculated extrapolating the Langmuir isotherm parameters in the low-pressure region (Eq.2). qi = qmax,i KL,iPi 1 + KL,iPi , KL,i = K0L,ie (− ΔHads,i RT) (1) KH,i = (∂ni ∂P) P→0 , SCO2 /N2 = KH,CO2 KH,N2 (2)

2.4.2. Fix bed adsorption

Fixed bed adsorption tests were performed in a packed bed coupled to a Varian 3380 gas chromatograph with a thermal conductivity detector (TCD) for online sampling (Fig. 2). The packed bed used was made up of two zones. The first is an inert area made up of wool and glass beads with a diameter of 2 mm; to minimize the dead volume of the installation and to improve dispersion of the gas mixture. The second one isan active zone constituted by the monolithic structure of activated carbon. The bed was activated at 120 ◦C overnight using a flow of 30 mL min− 1 of He. For adsorption kinetics, the temperature of the equipment was programmed at the same conditions as the adsorption isotherms (25, 40, and 65 ◦C). The studied gases (CO2 and N2) were adjusted to a flow of 5 mL min− 1 and diluted with helium until reaching total flow rates of 30, 60, and 90 mL min− 1 . The TCD sensor reference gas was set at 30 mL min− 1 , with oven and filament temperatures of 200 ◦C and 253 ◦C, respectively. For a typical experiment, He flowed for 5 min with the two-way valve set to position one to obtain the baseline for the measurement. Next, the valve was changed to position 2, entering the gas mixture into the bed until the signal in the detector was constant. Finally, for desorption, the system was placed in position one, and He was allowed to flow again until the sensor signal was zero. The adsorption capacity from the breakthrough curves was determined using a mass balance described by the following equation. qeq = QvCo (∫ ∞ 0 (1 − C Co) dt − tm) Wads (3) Where Qv is the experimental flow rate (m3 s − 1), Co the concentration of the studied gas (mol m− 3), ∫ ∞ 0 (1 − C Co) dt are the moles retained by the adsorbent, tm is the dead time of the system calculated from the breakthrough curves of He (s) (Fig. S2), and Wads is the mass of the adsorbent used (kg) (Table S1).

3. Results and discussion

3.1. Morphological properties of AC and AC monoliths

The manufactured monoliths present a microscopic structure similar to their precursor powders, comprised of agglomerated particles with an average diameter of around 1.5 μm (Fig. 3(a, b)). The macrostructures obtained with all nozzle diameters presented layers with symmetrical rods and a 90◦ contact angle between layers. Furthermore, the line-toline separation in each layer was homogeneous for

all structures, heights, and nozzle sizes (Fig. 3(c-f)). Therefore, indicate the correct ink dosage and selection of printing parameters in the proposed extrusion system. The printing parameters used by different authors are reported in Table 2. Compared to other 3D printed monoliths used for gas separation, the CA monoliths prepared in this work presented printing speeds of up to 7 mm/s, higher than other works reported with binder loads of the same magnitude. Likewise, a well-defined cell density per square inch was reached in the range of 108–1308; the monolith with the highest cell density had a wall diameter of 0.42 mm and a filling percentage of 70%. The preceding suggests adequate ink formulation and structuring methodology for CA powder 3D printing. Fig. 4 shows the variation in the dimensions of the monolithic structures in the different stages of manufacture. At the time of printing, the monoliths presented a deviation of less than 3% from the simulated structures for all heights and diameters, indicative of a good alignment between the printing speed and flow of the material deposited by the designed microextruder. As the monolith cured, the water in the printed paste volatilized, decreasing the monolith dimensions by 4% at room temperature and by 8% when heat-treated at 600 ◦C. Thus, to accommodate this shrinkage, structures must be designed with a size greater than that required for their intended use.

3.2. Physicochemical properties of AC and AC monoliths

The adsorption-desorption of nitrogen from the AC monoliths and powders (Fig. 5a) presented a type IV isotherm according to the IUPAC classification, characteristic of microporous and mesoporous materials [34]. Moreover, the isotherms have a type-H3 hysteresis curve at relative pressures greater than 0.44, as suggested by the presence of slit-shaped pores, which are characteristic of carbonaceous materials made from lignocellulosic precursors. The textural properties of AC powder and monoliths are shown in Table 3. ACm monoliths lost an average of 12% specific surface area and micropore volume compared to AC powder, possibly caused by partial pore blockage by the remaining carbon from the CMC in the pyrolysis process. On the other hand, the temperature increase in the thermal treatment in the CA monoliths caused an increase in the proportion of micropores smaller than 1 nm (Fig. 5b) associated with the thermal degradation of the CA (Fig. S1). This effect is desirable in applications such as CO2 adsorption, whose optimal pore range for adsorption is less than 1 nm [35,36]. The surface chemistry was evaluated from charge distribution and XPS analysis. Fig. 6 shows the load distributions of the AC and monoliths at different heat treatment temperatures. The isoelectric point increased with temperature from 6.39 for AC powder to 7.43 and 9.65 under heat treatment at 400 ◦C and 600 ◦C, respectively. This result indicates that the structuring of the material with CMC and its thermal treatment causes a reduction

in the proportion of acidic functional groups and the ratio of basic to acidic site changes. The above is corroborated by the increase in the C:O ratio and the decreases in the proportions of C– –O, COO, and O– –C acidic functional groups (Table 4) in the high-resolution C1s and O1s spectra (Fig. 7). The decrease in oxygenated groups with increasing heat treatment temperature agrees with the reports in the literature [37].

3.3. Compressive strength performance of AC monoliths

Fig. 8 shows the compressive strength of the evaluated materials. For all structures and heat treatments, two different regions were observed. The first region is an elastic region with up to 1% deformation. The second plastic region is divided into two zones: a zone of perfect creep up to 2.3%, followed by a hardening zone to the failure region of 4.5–6%. The monoliths evaluated presented compressive strengths of 0.58–3.53 MPa, which is on the same order of magnitude as those of other carbon monoliths used in gas separation and catalysis applications [38-40]. Statistical analysis (Table 5) revealed that the compressive strength depends on the infill percentage of the monoliths and increases proportionally to the monolith wall diameter and heat treatment temperature (Fig. 9). This structural tendency indicates that the material's resistance is centered on the outer wall of the monolith because of the structuring approach used: due to the fabrication of interspersed layers with an angle of 90◦, only the outer wall presents continuity, better distributing the load as the thickness increases, which allows it to withstand more significant stress. Furthermore, an increased heat treatment temperature results in considerable compaction, leading to a better distribution of forces throughout the monolith.

3.4. CO2 and N2 adsorption performance of AC structures

The CO2 and N2 adsorption equilibria at different temperatures for powdered and structured AC are presented in Fig. 10. For all ACs, the adsorption capacity of the gases studied presented an inversely proportional effect to the increase in temperature and enthalpies of adsorption in the range of 14–30 kJ, suggesting an adsorption process by weak interactions (physisorption). In order to compare the effect of CA structuring, the equilibrium adsorption capacity of the pellets and monoliths was obtained from the breakthrough curves (Fig. 11) using a mass bed balance described by Eq. (3). The adjusted parameters of the Langmuir isotherm are shown in Table 6. The maximum adsorption capacity of the structured CA (monolith and granules) decreased by 16% compared to the AC powder. The decrease in maximum capacity is associated with the loss in the textural properties of structured ACm, showing the same order of magnitude as the decrease in capacity. Although the loss is significant in the saturation pressure region, the materials structured in the form of monoliths presented similar adsorption capacity to their

powder counterpart in the low-pressure region. At low pressures, CO2 adsorption is controlled by the material's ultra-microporosity (pores <1 nm), which did not vary when structuring monolithically, as evidenced in the pore distribution (Fig. 5b).

One of the fundamental characteristics of a functional adsorbent is selectivity to specific adsorbates, and the limit selectivity measured by Henry's law gives a fair estimate when adsorbents are used at low pressures. Table 7 presents the Henry adsorption constant and selectivity of AC and AC in monolithic form. For all the temperatures evaluated, the selectivity did not present significant changes and therefore is independent of the structuring of the AC through 3D printing and the heat treatment.

3.4.1. Fix bed adsorption

In order to compare the efficiency in continuous gas separation processes, the monolith ACM_0.42_50_600 was compared to pellets with the same wall diameter. Fig. 11 presents the two evaluated structures' rupture curves at different CO2 feed fractions and temperatures. For all experiments, the monolithic structure of ACm presented rupture curves with steeper slopes compared to the structures in the form of pellets, i.e. a more negligible difference between the time to reach 5% (breakpoint) and 95% (saturation point) of the feed concentration in the outlet stream, as noted in Table 8. At room temperature and a fraction molar of 0.17, the CA monolith printed using 3D technology showed a decrease of approximately 21% in the difference between breakpoint and saturation point (t95%-t5%) compared to CA in the form of pellets. The previous confirms that the 3D printed monoliths evaluated have a lower mass transfer zone (MZT) than traditional packings with the same rod diameter and, therefore, lower global resistance to mass transfer.

4. Conclusions

The 3D printing method was used in a laboratory-scale study of monolithic structures of activated carbor from renewable sources. The effect of the binder and heat treatment on the textural, chemical, and mechanical properties of the activated carbon used was demonstrated. The monolithic structures presented a decrease of up to 12% in their textural properties compared to the AC powder precursor. The amount of acid functional groups on the activated carbon was inversely proportional to the heat treatment temperature. The structured activated carbons presented resistance to compression comparable with those of materials used in industry for gas separation and catalysis, with the heat treatment temperature and the wall thickness being the most critical parameters. The CO2 adsorption tests showed that the structuring by 3D printing did not affect the adsorption capacity and selectivity of the powder precursor in the low-pressure region. Likewise, the monolithic structuring presented a smaller mass transfer zone than conventional pellet packaging with the same wall diameter.

References

[1] V.I. Agueda, J.A. Delgado, M.A. Uguina, P. Brea, A.I. Spjelkavik, R. Blom, C. Grande, Adsorption and diffusion of H2, N2, CO, CH4 and CO2 in UTSA-16 metal-organic framework extrudates, Chem. Eng. Sci. 124 (2015) 159–169, https://doi.org/10.1016/j.ces.2014.08.039.

[2] F. Akhtar, L. Andersson, S. Ogunwumi, N. Hedin, L. Bergstrom, ¨ Structuring adsorbents and catalysts by processing of porous powders, J. Eur. Ceram. Soc. 34 (7) (2014) 1643–1666, https://doi.org/10.1016/j.jeurceramsoc.2014.01.008.

[3] S. Lawson, B. Adebayo, C. Robinson, Q. Al-Naddaf, A.A. Rownaghi, F. Rezaei, The effects of cell density and intrinsic porosity on structural properties and adsorption kinetics in 3D-printed zeolite monoliths, Chem. Eng. Sci. (2020) 218, https://doi.org/10.1016/j.ces.2020.115564.

[4] S.J.A. DeWitt, A. Sinha, J. Kalyanaraman, F. Zhang, M.J. Realff, R.P. Lively, Critical comparison of structured contactors for adsorption-based gas separations, Annu. Rev. Chem. Biomol. Eng. 9 (1) (2018) 129–152, https://doi.org/10.1146/annurevchembioeng-060817-084120.

[5] J.C. Ruiz-Morales, A. Tarancon, ´ J. Canales-Vazquez, J. M´endez-Ramos, L. Hernandez-Afonso, ´ P. Acosta-Mora, J.R. Marín Rueda, R. Fernandez-Gonzalez, Three dimensional printing of components and functional devices for energy and environmental applications, Energy Environ. Sci. 10 (4) (2017) 846–859, https://doi.org/10.1039/c6ee03526d.

[6] Y. Ma, F. Zhang, R.P. Lively, Manufacturing Nanoporous Materials for and Challenges. Sustainable Nanoscale Engineering, Elsevier Inc, 2020, https://doi.org/10.1016/B978-0-12-814681-1.00003-5.

[7] J. Lefevere, M. Gysen, S. Mullens, V. Meynen, J.V. Noyen, The benefit of design of support architectures for zeolite coated structured catalysts for methanol-to-olefin conversion, Catal. today 216 (2013) 18–23, https://doi.org/10.1016/j.cattod.2013.05.020.

[8] D.F.M. Santos, O.S.G.P. Soares, A.M.T. Silva, J.L. Figueiredo, M.F.R. Pereira, Degradation and mineralization of oxalic acid using catalytic wet oxidation over carbon coated ceramic monoliths, J. Environ. Chem. Eng. 9 (4) (2021), 105369, https://doi.org/10.1016/j.jece.2021.105369.

[9] Y. Zhang, Q. Wang, B. Louis, ZSM-5 zeolite coatings on perlite support for MTO application, Microporous Mesoporous Mater. 323 (2021), 111172, https://doi.org/10.1016/j.micromeso.2021.111172.

[10] J. Lefevere, L. Protasova, S. Mullens, V. Meynen, 3D-printing of hierarchical porous ZSM-5: the importance of the binder system, Mater. Des. 134 (2017) 331–341, https://doi.org/10.1016/j.matdes.2017.08.044.

[11] Ozbolat, I.T. (2017). Extrusion-Based Bioprinting * *With minor contributions by Monika Hospodiuk, The Pennsylvania State University. In 3D Bioprinting. https://doi.org/10.1016/b978–0-12–803010-3.00004–4.

[12] J. Liu, H. Shang, J. Yang, J. Wang, J. Li, S. Deng, Novel zeolite/carbon monolith adsorbents for efficient CH4/N2 separation, Chem. Eng. J. 426 (June) (2021), 130163, https://doi.org/10.1016/j.cej.2021.130163.

[13] J. Singh, H. Bhunia, S. Basu, Journal of the Taiwan Institute of Chemical Engineers Synthesis of porous carbon monolith adsorbents for carbon dioxide capture: breakthrough adsorption study, J. Taiwan Inst. Chem. Eng. 89 (2018) 140–150, https://doi.org/10.1016/j.jtice.2018.04.031.

[14] S. Govender, H. Friedrich, Monoliths: a review of the basics, preparation methods and their relevance to oxidation, Catalysts 7 (12) (2017) 62, https://doi.org/10.3390/catal7020062.

[15] B. Verougstraete, D. Schuddinck, J. Lefevere, G.V. Baron, J.F.M. Denayer, A 3Dprinted zeolitic imidazolate framework-8 monolith for flue- and biogas separations by adsorption: influence of flow distribution and process parameters, Front. Chem. Eng. 2 (November) (2020) 1–8, https://doi.org/10.3389/fceng.2020.589686.

[16] S. Couck, J. Cousin-Saint-Remi, S. Van der Perre, G.V. Baron, C. Minas, P. Ruch, J. F.M. Denayer, 3D-printed SAPO-34 monoliths for gas separation, Microporous Mesoporous Mater. 255 (2018) 185–191, https://doi.org/10.1016/j.micromeso.2017.07.014.

[17] U. Simon, S. Dimartino, Direct 3D printing of monolithic ion exchange adsorbers, J. Chromatogr. A 1587 (2019) 119–128, https://doi.org/10.1016/j.chroma.2018.12.017.

[18] B. Bian, D. Shi, X. Cai, M. Hu, Q. Guo, C. Zhang, Q. Wang, A.X. Sun, J. Yang, 3D printed porous carbon anode for enhanced power generation in microbial fuel cell, Nano Energy 44 (2018) 174–180, https://doi.org/10.1016/j.nanoen.2017.11.070.

[19] S. Couck, J. Lefevere, S. Mullens, L. Protasova, V. Meynen, G. Desmet, G.V. Baron, J.F.M. Denayer, CO2, CH4 and N2 separation with a 3DFD-printed ZSM-5 monolith, Chem. Eng. J. 308 (2017) 719–726, https://doi.org/10.1016/j.cej.2016.09.046.

[20] A. Quintanilla, J.A. Casas, P. Miranzo, M.I. Osendi, M. Belmonte, 3D-Printed Fedoped silicon carbide monolithic catalysts for wet peroxide oxidation processes, Appl. Catal. B: Environ. 235 (February) (2018) 246–255, https://doi.org/10.1016/j.apcatb.2018.04.066.

[21] M.J. Regufe, A.F.P. Ferreira, J.M. Loureiro, A. Rodrigues, A.M. Ribeiro, Electrical conductive 3D-printed monolith adsorbent for CO 2 capture, Microporous Mesoporous Mater. 278 (October 2018) (2019) 403–413, https://doi.org/10.1016/j.micromeso.2019.01.009.

[22] H. Thakkar, S. Eastman, Q. Al-Naddaf, A.A. Rownaghi, F. Rezaei, 3D-printed metalorganic framework monoliths for gas adsorption processes, ACS Appl. Mater. Interfaces 9 (41) (2017) 35908–35916, https://doi.org/10.1021/acsami.7b11626.

[23] R.M. Hensleigh, H. Cui, J.S. Oakdale, J.C. Ye, P.G. Campbell, E.B. Duoss, C. M. Spadaccini, X. Zheng, M.A. Worsley, Additive manufacturing of complex microarchitected graphene aerogels, Mater. Horiz. 5 (6) (2018) 1035–1041, https://doi.org/10.1039/c8mh00668g.

[24] H. Steldinger, A. Esposito, K. Brunnengraber, J. Glasel, B.J.M. Etzold, Activated carbon in the third dimension—3D printing of a tuned porous carbon, Adv. Sci. 6(19) (2019), https://doi.org/10.1002/advs.201901340.

[25] A. Szczurek, A. Ortona, L. Ferrari, E. Rezaei, G. Medjahdi, V. Fierro, D. Bychanok, P. Kuzhir, A. Celzard, Carbon periodic cellular architectures, Carbon 88 (2015)70–85, https://doi.org/10.1016/j.carbon.2015.02.069.

[26] L.F.A.S. Zafanelli, A. Henrique, H. Steldinger, J.L. Diaz de Tuesta, J. Glasel, A.E. Rodrigues, H.T. Gomes, B.J.M. Etzold, J.A.C. Silva, 3D-printed activated carbon for post-combustion CO2 capture, Microporous Mesoporous Mater. (2022) 335, https://doi.org/10.1016/j.micromeso.2022.111818.

[27] S. Chandrasekaran, B. Yao, T. Liu, W. Xiao, Y. Song, F. Qian, C. Zhu, E.B. Duoss, C. M. Spadaccini, Y. Li, M.A. Worsley, Direct ink writing of organic and carbon aerogels, Mater. Horiz. 5 (6) (2018) 1166–1175, https://doi.org/10.1039/c8mh00603b.

[28] X. Tang, H. Zhou, Z. Cai, D. Cheng, P. He, P. Xie, D. Zhang, T. Fan, Generalized 3D printing of graphene-based mixed-dimensional hybrid aerogels, ACS Nano 12 (4) (2018) 3502–3511, https://doi.org/10.1021/acsnano.8b00304.

[29] A. Mantelli, A. Romani, R. Suriano, M. Levi, S. Turri, Direct ink writing of recycled composites with complex shapes: process parameters and ink optimization, Adv. Eng. Mater. (2021), https://doi.org/10.1002/adem.202100116.

[30] K. Pusch, T.J. Hinton, A.W. Feinberg, HardwareX Large volume syringe pump extruder for desktop 3D printers, HardwareX 3 (November 2017) (2018) 49–61, https://doi.org/10.1016/j.ohx.2018.02.001.

[31] C.B. García-Reyes, J.J. Salazar-Rabago, M. Sanchez-Polo, M. Loredo-Cancino, R. Leyva-Ramos, Ciprofloxacin, ranitidine, and chlorphenamine removal from aqueous solution by adsorption. Mechanistic and regeneration analysis, Environ. Technol. Innov. 24 (2021), 102060, https://doi.org/10.1016/j.eti.2021.102060.

[32] ASTM International. (2015). Standard Test Method for Compressive Strength of Carbon and Graphite. In ASTM International (Vol. 03, pp. 1–13). https://doi.org/10.1520/C0695–15R20.

[33] D.C. Montgomery, Diseno y analisis de experimentos, Limusa Wiley, 2005.

[34] Thommes, M., Kaneko, K., Neimark, A.V., Olivier, J.P., Rodriguez-reinoso, F., Rouquerol, J., & Sing, K.S.W. (2015). Physisorption of gases, with special reference to the evaluation of surface area and pore size distribution (IUPAC Technical Report). 87, 1051–1069. https://doi.org/10.1515/pac-2014–1117.

[35] J. Srenscek-Nazzal, ´ K. Kiełbasa, Advances in modification of commercial activated carbon for enhancement of CO2 capture, Appl. Surf. Sci. 494 (June) (2019) 137–151, https://doi.org/10.1016/j.apsusc.2019.07.108.

[36] H. Yuan, J. Chen, D. Li, H. Chen, Y. Chen, 5 Ultramicropore-rich renewable porous carbon from biomass tar with excellent adsorption capacity and selectivity for CO2 capture, Chem. Eng. J. 373 (2) (2019) 171–178, https://doi.org/10.1016/j.cej.2019.04.206.

[37] M. Smith, L. Scudiero, J. Espinal, J.S. McEwen, M. Garcia-Perez, Improving the deconvolution and interpretation of XPS spectra from chars by ab initio calculations, Carbon 110 (2016) 155–171, https://doi.org/10.1016/j.carbon.2016.09.012.

[38] A. Arami-Niya, T.E. Rufford, Z. Zhu, Activated carbon monoliths with hierarchical pore structure from tar pitch and coal powder for the adsorption of CO2, CH4 and N2, Carbon 103 (2016) 115–124, https://doi.org/10.1016/j.carbon.2016.02.098.

[39] P.O. Ibeh, F.J. García-Mateos, J.M. Rosas, J. Rodríguez-Mirasol, T. Cordero, Activated carbon monoliths from lignocellulosic biomass waste for electrochemical applications, J. Taiwan Inst. Chem. Eng. 97 (2019) 480–488, https://doi.org/10.1016/j.jtice.2019.02.019.

[40] D. Lozano-Castello, ´ D. Cazorla-Amoros, ´ A. Linares-Solano, D.F. Quinn, Activated carbon monoliths for methane storage: influence of binder, Carbon 40 (15) (2002) 2817–2825, https://doi.org/10.1016/S0008-6223(02)00194-X.

FIGURES

Fig. 1. Mechanical piston microextruder.

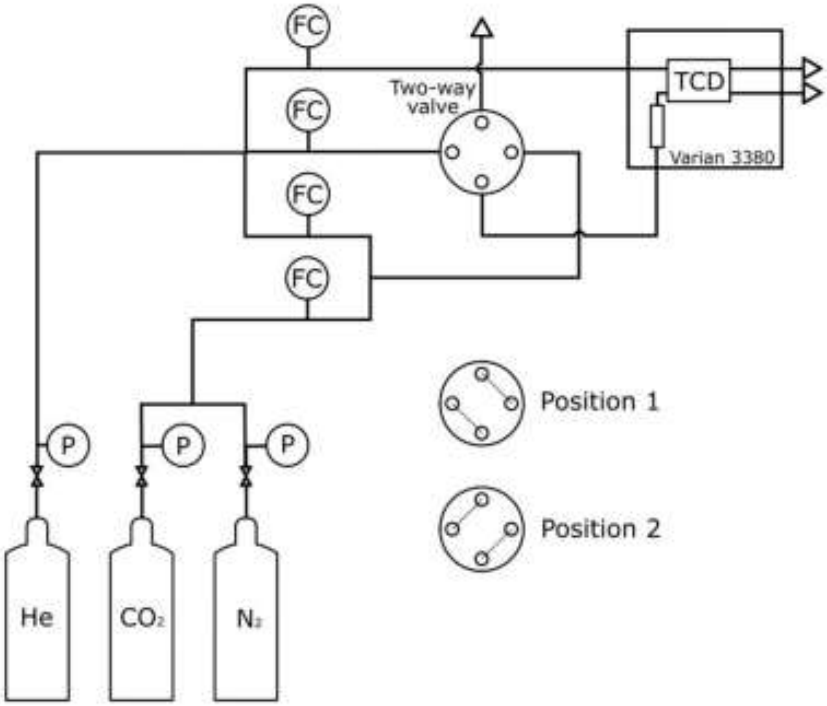

Fig. 2. Scheme of the setup for fixed bed adsorption measurements.

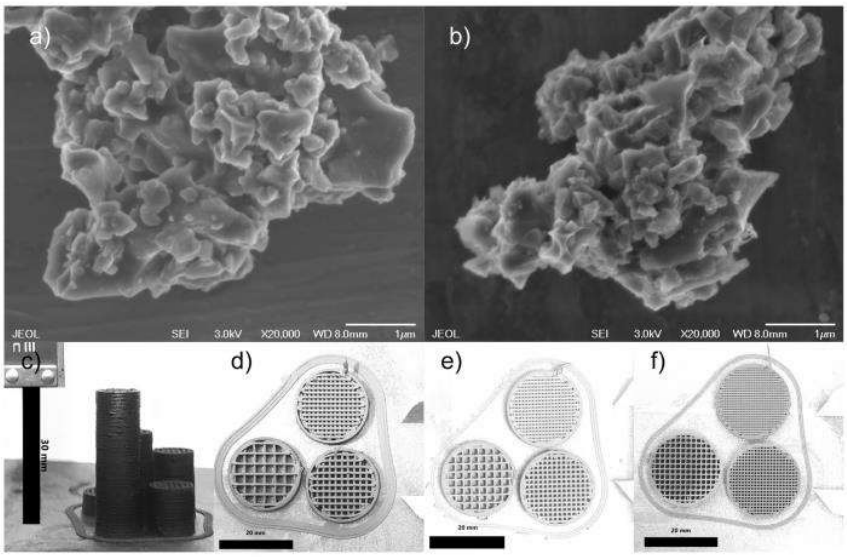

Fig. 3. SEM images of a) AC powder, b) AC monoliths thermally treated at 600 °C, c) AC monoliths printed at different heights (5–30 mm) with a diameter = 10 mm, and monoliths with different infill percentages and nozzle sizes: d) 0.82 mm, e) 0.62 mm, and f) 0.42 mm.

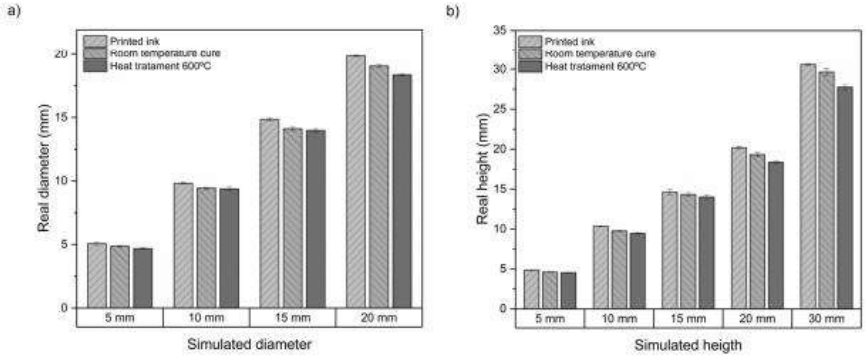

Fig. 4. Monolith dimensions in different manufacturing stages: a) diameter and b) height.

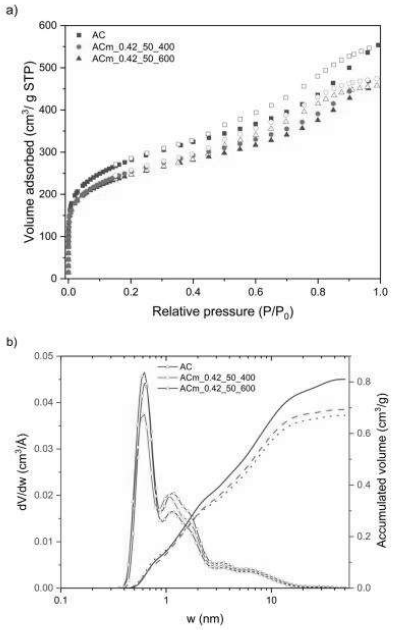

Fig. 5. a) Nitrogen physisorption isotherms at − 196.15 °C (full markers adsorption, empty markers desorption) and b) pore distribution of powdered AC and AC monoliths.

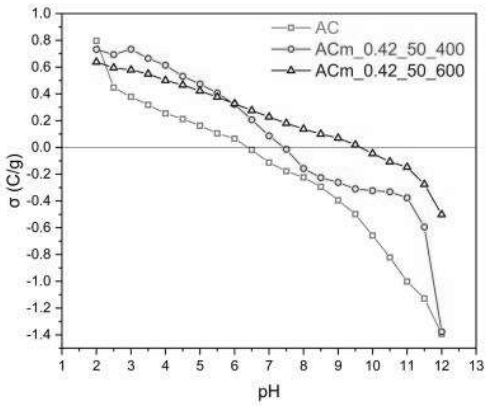

Fig. 6. Activated carbon surface charge as a function of pH.

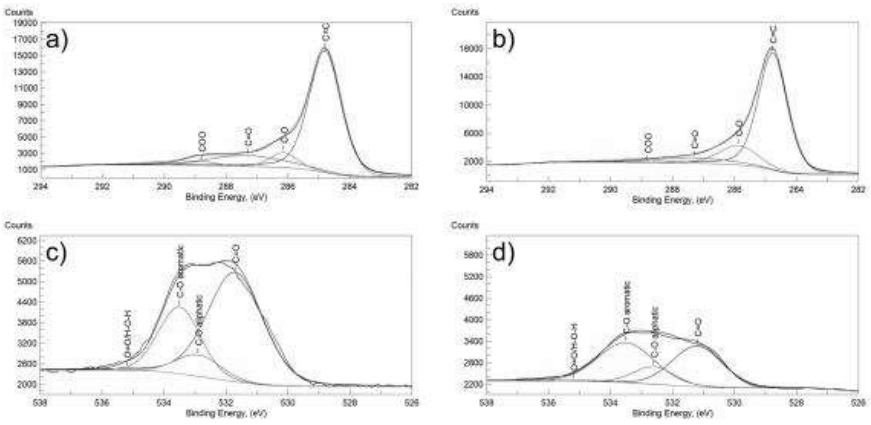

Fig. 7. High-definition scans of C1s of a) AC and b) AC_0.42_50_600 and O1s of c) AC and d) AC_0.42_50_600.

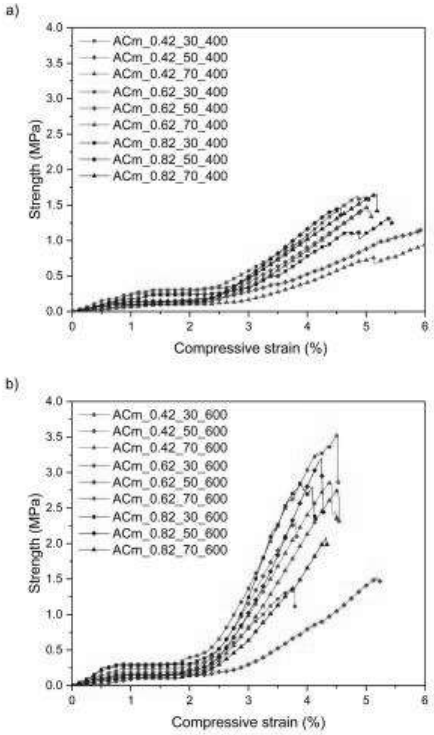

Fig. 8. Compressive strength of monoliths treated at different temperatures: a) 400 °C and b) 600 °C.

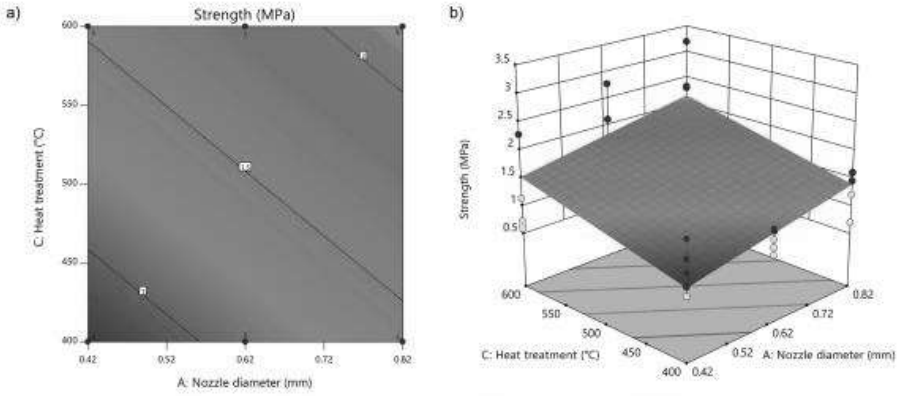

Fig. 9. a) Contour plot and b) response surface of resistance to compression of 3D printed carbon monoliths.

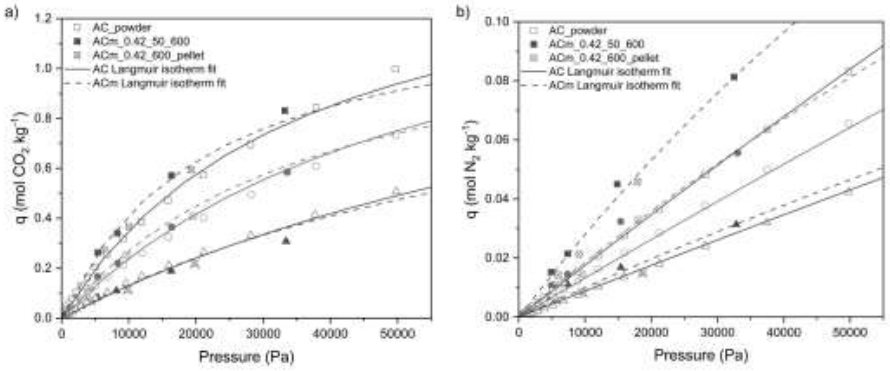

Fig. 10. a) CO_2 and b) N_2 isotherms on the obtained samples at three different temperatures (black 25ºC, red 40ºC and blue 65ºC) and the Langmuir model.

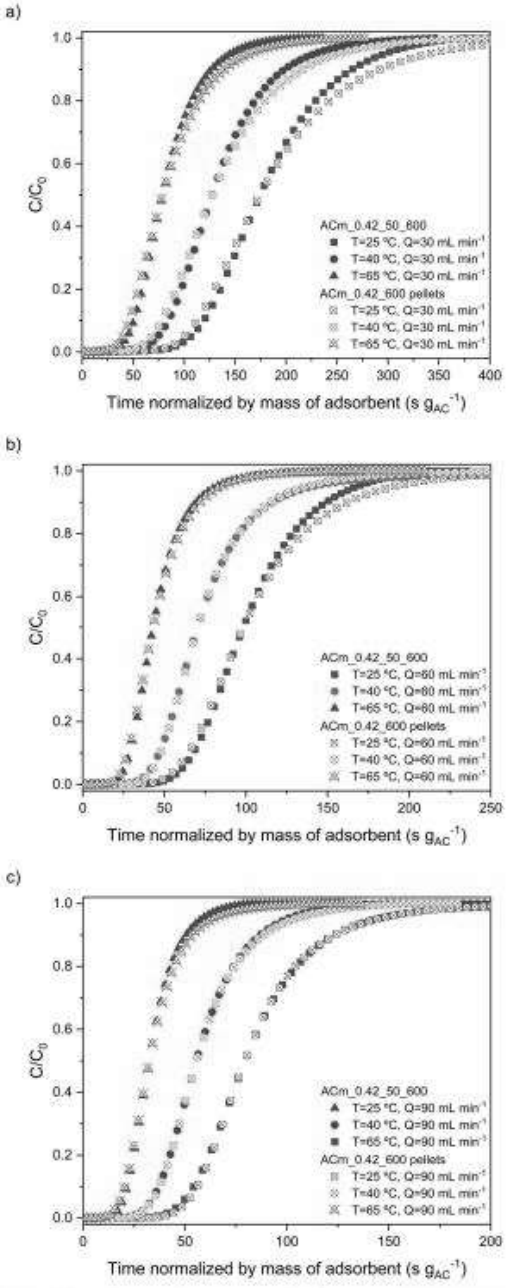

Fig. 11. Breakthrough curves of CO_2 in activated carbon X_{CO2}= a) 0.17 b) 0.08 c) 0.06.

TABLES

Table 1
Multilevel factorial design of the mechanical strength of AC monoliths.

Independent variable	Coded factor	Coded levels		
		-1	0	1
		Actual levels		
Nozzle diameter (mm)	A	0.42	0.62	0.82
Infill percentage (%)	B	30	50	70
Heat treatment temperature (°C)	C	400	500	600

Table 2
Summary of 3D-printed structured materials.

Primary component	Plasticizer	Binder (ratio)	Printing conditions	Ref.
Zeolite SAPO-34	Polyacrylic acid 0.6% Methylcellulose 2–3%	48%w/w 48% w/w + 4% graphite	V= 4 mm/s ØB= 330 μm Ts= 25 °C ts= 48 h	[16]
ZSM-5	Bentonite 17.5% Colloidal silica 17.5%	35%w/w	V= N.R. ØB= 400–900 μm Ts= 20 °C 80% HR ts= 24 h	[19]
ZSM-5	Bentonite Silica Methylcellulose 0.5% Aluminophosphate solution 1%	37–65% w/w	V= 1.58 mm/s ØB= 900 μm Ts= 20 °C 80% HR ts=N.R.	[10]
Zeolite 13X and activated carbon MCS-30	Carboxy- methylcellulose 3.5%	60% w/w	V=N.R. ØB= 840 μm Ts= 20 °C ts= 48 h	[21]
Activated carbon LS-325	Carboxy- methylcellulose 3%	63% w/w	V= 7 mm/s ØB= 420–820 μm Ts= 25 °C ts= 24 h	This work

V: Printing speed, ØB: Nozzle diameter, Ts: Drying temperature, ts: Drying time, N.R.: Not reported

Table 3
Textural properties of AC powder and monoliths.

Sample	S_{BET} (m^2g^{-1})	V_{mic} (cm^3g^{-1})	V_T (cm^3g^{-1})	D_{ar} (Å)
AC	1006	0.318	0.810	6.4
ACm_0.42_50_400	905	0.291	0.693	6.2
ACm_0.42_50_600	882	0.287	0.670	6.1

Table 4
High-definition scan C1s and O1s peak parameters with deconvolution.

Total peak area	AC	AC_0.42_50_600
C1s (CPS.ev)	31039	30225
O1s (CPS.ev)	12817	6114
C:O*	6.52	12.89
C1s deconvolution (atomic %)		
C=C	73.1	74
C-O	7.8	16.5
C=O	16.6	9.1
COO	2.5	0.4
O1s deconvolution (atomic %)		
aromatic O-C	27.6	43.9
aliphatic O-C	9.5	14.1
C=O	62.2	39.7
O_2/H_2O	0.6	2.3

Table 5
Analysis of variance data for the mechanical strength of the monoliths.

Source	Sum of squares	Degrees of freedom	Mean square	F value	p value	
Model	21.1	5	4.21	23.2	< 0.0001	significant
A-Nozzle diameter	5.69	1	5.69	31.5	< 0.0001	
B-Infill percentage	0.462	1	0.462	2.55	0.1138	
C-Heat treatment temperature	12.66	1	12.6	69.9	< 0.0001	
AB	0.736	1	0.736	4.07	0.0469	
ABC	1.57	1	1.57	8.70	0.0041	
Residual	15.0	83	0.181			
Lack of fit	2.47	12	0.206	1.16	0.3263	not significant
Pure error	12.5	71	0.177			
Cor total	36.1	88				

Table 6
Parameters of the Langmuir isotherm in the adsorption of CO_2 and N_2 in AC adsorbents.

Adsorbed molecule	Adsorbent	Parameter	Value±SE[a]	95% confidence limit		R^2_{adj}	RMSE[b]
				Lower limit	Upper limit		
CO_2	AC_powder	q_{max} (mol kg^{-1})	1.61 ± 0.256	1.21	2.25	0.957	0.202
		$K_0 x10^{-10}$ (Pa^{-1})	15.8 ± 8.22	5.43	45.6		
		$\Delta_{ads} x10^3$ (J mol^{-1})	-24.2 ± 1.44	-27.1	-21.4		
	ACm_0.42_0.5_600 ACm_0.42_600_pellets	q_{max} (mol kg^{-1})	1.35 ± 0.136	1.02	1.59	0.984	0.0756
		$K_0 x10^{-10}$ (Pa^{-1})	3.32 ± 1.38	0.430	6.21		
		$\Delta_{ads} x10^3$ (J mol^{-1})	-29.4 ± 1.30	-32.1	-26.6		
N_2	AC_powder	q_{max} (mol kg^{-1})	1.61 ± 0.315	1.16	2.65	0.999	5.04 $x10^{-3}$
		$K_0 x10^{-10}$ (Pa^{-1})	31.1 ± 5.54	19.7	42.0		
		$\Delta_{ads} x10^3$ (J mol^{-1})	-14.6 ± 0.176	-14.9	-14.2		
	ACm_0.42_0.5_600 ACm_0.42_600_pellets	q_{max} (mol kg^{-1})	0.479 ± 0.226	0.277	5.35	0.981	0.704
		$K_0 x10^{-10}$ (Pa^{-1})	6.97 ± 3.81	1.09	21.7		
		$\Delta_{ads} x10^3$ (J mol^{-1})	-23.3 ± 1.17	-25.7	-19.2		

[a] Standard Error,
[b] Normal Root Mean Square Error

Table 7
Henry adsorption constant and adsorption selectivity of activated carbon.

Temperature °C	Henry adsorption constant (mol Kg^{-1} Pa^{-1})				Selectivity (molCO_2 molN_2^{-1})	
	$K_{HCO2} x10^{-6}$		$K_{HN2} x10^{-6}$		K_{HCO2}/K_{HN2}	
	ACm_0.42_50_600	AC_powder	ACm_0.42_50_600	AC_powder	ACm_0.42_50_600	AC_powder
25	44.4	63.8	1.81	2.66	24.5	24.0
40	27.8	36.1	1.37.	1.73	20.3	20.9
65	14.0	15.7	0.90	0.91	15.5	17.1

Table 8
Breakthrough time ($t_{5\%}$) and saturation time ($t_{95\%}$) per gram of adsorbent.

Adsorbent	X_{CO2}	Temperature	$t_{5\%}$ (s)	$t_{95\%}$ (s)	$t_{95\%}$-$t_{5\%}$ (s)
ACm_0.42_50_600	0.17	25	106.4	296.8	190.3
		40	74.3	228.2	153.8
		65	44.4	145.6	101.2
	0.08	25	60.6	167.9	107.2
		40	41.8	140.7	98.9
		65	25.3	81.9	56.6
	0.06	25	48.3	143.2	94.9
		40	32.9	99.6	66.7
		65	19.1	57.9	38.8
AC_0.42_600_pellets	0.17	25	100.2	340.9	240.7
		40	68.3	251.8	183.5
		65	39.8	164.7	124.9
	0.08	25	57.1	190.4	133.3
		40	42.7	137.1	94.4
		65	24.2	84.8	60.6
	0.06	25	50.4	144.1	93.6
		40	33.1	103.0	69.9
		65	17.6	63.5	45.9